Available online at www.sciencedirect.com
ScienceDirect
Journal of Solid State Chemistry 181 (2008) 1040–1047
JOURNAL OF SOLID STATE CHEMISTRY
www.elsevier.com/locate/jssc

Correlation between structural features and vis–NIR spectra of α-Fe_2O_3 hematite and AFe_2O_4 spinel oxides (A = Mg, Zn)

N. Pailhé, A. Wattiaux, M. Gaudon*, A. Demourgues

Bordeaux Institute of Condensed Matter Chemistry, ICMCB-CNRS, 87 Avenue du Dr. Albert Schweitzer, 33608 Pessac Cedex, France

Received 10 January 2008; received in revised form 7 February 2008; accepted 8 February 2008
Available online 23 February 2008

Abstract

Iron (III) rich pigments $MgFe_2O_4$ and $ZnFe_2O_4$ spinel ferrites and α-Fe_2O_3 hematite were synthesized by Pechini route and precipitation process, respectively. The compounds were characterized by X-ray diffraction (XRD), Mössbauer spectroscopy and visible–NIR spectroscopy. Diffuse reflectance spectra were interpreted in regard of structural features of the three oxides in order to correlate absorption bands positions with structural parameters. It has been demonstrated that the two main absorption edges occurring in visible range (400–800 nm) can be attributed to two $2p(O^{2-})\rightarrow 3d(Fe^{3+})$ charge transfers, the energy being directly linked to the distortion degree of the [FeO_6] octahedra.

Keywords: Red pigments; Spinel ferrites; Hematite; Structural features; Charge transfers; *d–d* Transitions

1. Introduction

Iron oxides and spinel ferrites are inorganic materials used in important industrial applications as color pigments, magnetic displays in recording media, catalysts, etc. Actually, such oxides are mainly used as pigments stable at high temperatures ($T>1000\,^{\circ}C$) to color up porcelain and ceramics [1,2]. α-Fe_2O_3 hematite is widely used as red pigment for Japanese porcelain enamel [3], $MgFe_2O_4$ pigment is nowadays commercially used as oil paint [4], $ZnFe_2O_4$ brown pigment has elsewhere been evaluated as a good infrared absorbing material [5]. α-Fe_2O_3 powders are mainly produced either by dehydration of goethite or thermal decomposition of natural $FeSO_4\cdot 7H_2O$ [3,6]. The conventional preparation of iron-rich spinel pigments is solid state route with temperature higher than 1000 °C [7]. In order to improve the powders performances, chemical methods as polymeric precursors and precipitation routes have been investigated in the last years. Indeed, these low-temperature routes allow a morphology control (grain size and shape), which can impact the powder coloration [8].

The intense reddish-brown color observed in case of these iron-rich oxides is entirely due to the Fe^{3+} chromophore cation. In literature, most of the authors do not take into account the ligand-to-metal $2p(O^{2-})\rightarrow 3d(Fe^{3+})$ charge transfer to explain the origin of this reddish color [9]. Actually for hematite, each absorption phenomenon in UV–visible region is interpreted considering $Fe^{3+}(3d^5)$ crystal-field transitions which are allowed thanks to the Fe^{3+}–Fe^{3+} anti-ferromagnetic coupling [10]. Nevertheless, several points about the crystal-field approach still are questionable. The present paper proposes to establish a clear correlation between diffuse reflectance spectra and structural data of $MgFe_2O_4$, $ZnFe_2O_4$ and α-Fe_2O_3 compounds. In particular, the octahedral site distortion has been considered here at the origin of the double ligand-to-metal $2p(O^{2-})\rightarrow 3d(Fe^{3+})$ charge transfer located in visible region and so responsible for the compounds reddish color.

2. Experimental details

2.1. Synthesis process

$ZnFe_2O_4$ and $MgFe_2O_4$ pigments were synthesized by the Pechini route [11]. This chemical process is based on

*Corresponding author.
E-mail address: gaudon@icmcb-bordeaux.cnrs.fr (M. Gaudon).

0022-4596/$ - see front matter © 2008 Elsevier Inc. All rights reserved.
doi:10.1016/j.jssc.2008.02.009

cations chelation by citric acid (CA) and on polyesterification between CA and ethylene glycol (EG) which leads to the formation of a polycationic resin. Aqueous solutions of citrate were prepared by dissolving CA ($C_6H_8O_7$, Sigma-Aldrich) in a minimal volume of water. Then, cationic salts: $Fe(NO_3)_3 \cdot 9H_2O$ and $Zn(NO_3)_2 \cdot 6H_2O$ or $Mg(NO_3)_2 \cdot 6H_2O$ (Sigma-Aldrich) were added in stoichiometric proportion to the acid solution. CA/cations precursors' molar ratio equal to 3/1 was used. After complete dissolution of metallic salts, EG ($C_2H_6O_2$, Sigma-Aldrich) was added with a 4/1 EG/CA molar ratio. EG–CA polymerization was promoted by removing water with continued heating on a hot plate. Then, the highly viscous mixtures were thermally treated in two steps: a first calcination at 300 °C for 10 h, then, an annealing for 5 h at 800 °C.

α-Fe_2O_3 compound was prepared using the precipitation of a hematite precursor from the addition of a basic media (NH_4OH aqueous solution) to a ferric nitrate solution ($Fe(NO_3)_3 \cdot 9H_2O$; Aldrich). The chemical composition of the amorphous precipitate still controversial, several authors thinking currently that $Fe(OH)_3$ iron hydroxide does not exist and that the precipitate can be rather considered as a poorly crystallized hydrated oxide ($Fe_2O_3 \cdot nH_2O$ ferrihydrite [12]). A pH of 9.5 was used according to the Pourbaix diagram [13], Fe^{3+} hydroxide being stable for pH between 4.5 and 10. In order to obtain the α-Fe_2O_3 oxide, a thermal treatment at 800 °C for 5 h under air was performed.

2.2. X-ray powder diffraction

A Philips PW 1820 apparatus equipped with a Cu($K\alpha_1$/$K\alpha_2$) source ($\lambda_{average} = 1.5424$ Å) was used to evaluate crystalline structure of all synthesized compounds. Diffraction patterns were collected with a 2θ step of 0.02° with a counting time of 10 s per step. For more advanced structural investigations, X-ray diffraction (XRD) measurements were carried out on a PANalytical X'PERT PRO diffractometer equipped with a X-celerator detector, using Co($K\alpha_1/K\alpha_2$) radiation ($\lambda_{average} = 1.7909$ Å) to limit the fluorescence of Fe. XRD data were recorded with a 2θ step = 0.017°. Diffractograms have been refined with Rietveld refinement method [14] using FULLPROF® program package [15]. Unit cell parameters, atomic positions, occupancies and Debye Weller factors have been refined. We assume that the spinel compounds exhibits strictly the Zn(or Mg)Fe_2O_4 formulae, hence constraint on occupancy factors was applied in order to respect this formulae integrity, i.e. the only variable which was refined is the inversion rate x defined as in $[Zn_{1-x}Fe_x]_{Td}(Zn_xFe_{2-x})_{Octa}O_4$ formulae.

2.3. Mössbauer spectroscopy

^{57}Fe Mössbauer measurements were performed at 293 K on a conventional constant acceleration spectrometer (HALDER) using rhodium matrix source. The spectra refinement was performed in two steps. First, the fitting of Mössbauer patterns as a series of Lorentzian profile peaks allowed the calculation of isomer shift (δ), amplitude and width (Γ) of each peak: thus, experimental hyperfine parameters were determined for the different iron sites (e.g. O_h and T_d). Secondly, spectra analysis was made in terms of quadrupolar splitting distribution $P(\Delta)$ and/or hyperfine field distribution $P(H)$ using the Hesse and Rubartsch method [16]; Γ and δ were fixed at values determined in the first refinement.

2.4. Diffuse reflectance measurements

The visible–NIR spectroscopies were carried out in diffuse reflectance mode on a VARIAN CARY 5000 spectrophotometer equipped with an integrating sphere coated with polytetrafluoroethylene (PTFE). Measurements were performed for wavelengths varying from 200 up to 2000 nm. HALON was used as white reference.

3. Results and discussion

3.1. Structural features of both types of compounds

The $MgFe_2O_4$ and $ZnFe_2O_4$ phases adopt a cubic symmetry with the *Fd*-3*m* space group related to the spinel-type structure. In such a structure, cations can occupy either octahedral (16*d*) or tetrahedral (8*a*) sites depending on their affinity for these various environments [17–19]; the spinel is defined as direct one when all divalent cations occupy tetrahedral sites while as octahedral sites are occupied by a fraction or the totality of divalent cations, the spinel structure is called partially inverted or fully inverted, respectively. Moreover, besides coloration interpretation of the oxides, one should have to mention that octahedral sites exhibit a loss of symmetry with a centrosymmetric D_{3d} point group. The α-Fe_2O_3 phase adopts rhombohedral symmetry with *R*-3*c* space group related to the corundum-type structure. The iron cations are located in octahedral site exhibiting a C_{3v} configuration, i.e. a more distorted configuration than spinel octahedral sites. Indeed, in C_{3v} configuration, the metallic cation is displaced along the three-fold axis from the geometric center of the octahedral site. Furthermore, the octahedra exhibit two equilateral triangles with different area along the three-fold axis, whereas in D_{3d} octahedra, the two equilateral faces are equivalent.

The XRD patterns of the samples annealed at 800 °C were analyzed according to JCPDS 79-0007 [20], 36-0398 [21] and 22-1012 [22]: pure phases have been always obtained with the expected structure. From the integral width of the diffraction patterns peaks ($\beta_{experimental}$), an evaluation of crystallite size by Sherrer formula, taking into account the instrumental contribution ($\beta_{instrument}$), indicates an average value of about 60, 80 and 165 nm for α-Fe_2O_3, $MgFe_2O_4$ and $ZnFe_2O_4$ compounds, respectively.

Thus, particles sizes of the three synthesized oxides are roughly comparable and are distinctly above the Bohr radius of oxides, around 5 nm. No quantum confinement can then be observed and so diffuse reflectance curves can be directly correlated to the structural features of such compounds. Moreover, Rietveld refinements were performed on these three compositions. As example, refinement plots (experimental, theory and difference) of $MgFe_2O_4$ sample are presented in Fig. 1 in order to show the quality of the refinement. For both phases, cell parameters, reliability factors, atomic positions, isotropic thermal displacement and occupancies are reported in Table 1. Furthermore, average oxygen–metal distances were compiled from the different structure refinements and are reported in Table 2. For the α-Fe_2O_3 corundum structure, refinements are in good agreement with those mentioned in literature [23], the reliability factors and isotropic thermal displacements values giving correct results. In case of spinel ferrites, results from occupancy refinements show that a high inversion rate is found for $MgFe_2O_4$ composition: the inversion rate is about 80%, which corresponds roughly to an inverted spinel network. On the contrary, an almost normal spinel network was obtained for $ZnFe_2O_4$ composition, the inversion rate being about equal to 15%. The averages O–cations bond distances in tetrahedral confirm that $ZnAl_2O_4$ spinel is almost a direct one (the O–cation distance in Td site is about the one predicted for Zn^{2+}–O^{2-} bonds in four-coordinance), whereas $MgFe_2O_4$ is almost an inverse one (the O–cation distance in T_d site is about the one predicted for Fe^{3+}–O^{2-} bonds in four-coordinance). One can notice that these results correspond to those mentioned in literature: indeed, $ZnFe_2O_4$ and $MgFe_2O_4$ are mainly referenced as normal-type and 90% inverse-type spinels, respectively [16,24–28]. Then X-ray data analyses show clearly that Fe^{3+} cations can occupy either tetrahedral of octahedral sites (with T_d and D_{3d} local point groups, respectively). Nevertheless, because of this partial occupation of Fe^{3+} in both sites it is also difficult from refinements to obtain information on local Fe^{3+} cations environments.

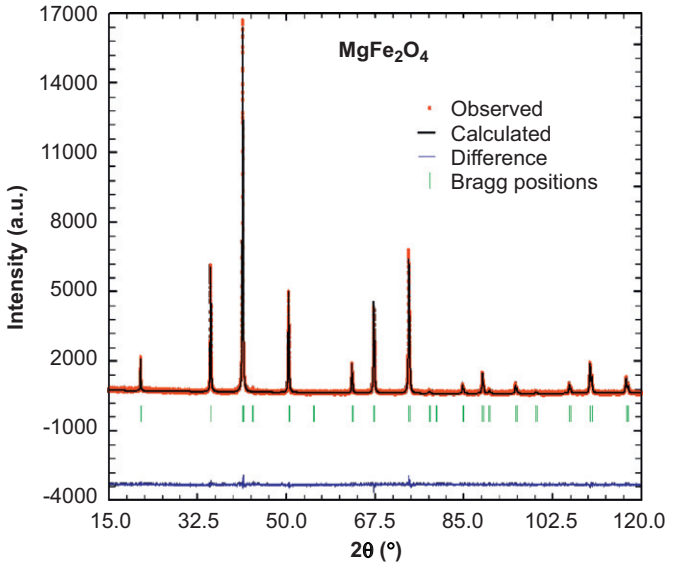

Fig. 1. Powder Rietveld refinement of $MgFe_2O_4$ sample. The lowest line is the difference between the calculated and experimental data. *Source*: Co($K\alpha_1/K\alpha_2$)

3.2. Mössbauer investigations

^{57}Fe Mössbauer measurements were performed on both spinel-type compounds. Firstly, on the basis of the refinement of each Mössbauer spectrum, the purity of samples has been demonstrated and no traces of Fe^{2+} have been detected. Experimental spectrum of zinc spinel shows a quadrupolar doublet, characteristic of a paramagnetic compound (Fig. 2a). This is in agreement with Néel temperature announced by literature (T_N referred about 10 K). As far as $MgFe_2O_4$ compound is concerned, experimental spectrum (Fig. 2a) can be described by a superposition of a major magnetic contribution (anti-ferromagnetic sextuplet, the T_N being about 650 K) and a minor paramagnetic contribution (quadrupolar doublet); this last phenomenon could be probably linked to the presence of sub-micron sized particles inducing a super-paramagnetism phenomenon in good agreement with smaller coherent domain (80 nm). One can notice that the paramagnetism behavior at room temperature of the $ZnFe_2O_4$ spinel besides the anti-ferromagnetism ordering of the $MgFe_2O_4$ spinel is consistent with J_{AB} exchange interactions stronger than J_{BB} ones where A and B correspond to tetrahedral and octahedral sites, respectively [29].

Hyperfine parameters of spinel ferrites are reported in Table 3. These results are in good agreement with literature [30,31]. In case of $ZnFe_2O_4$, the inversion rate calculated around 10% is in good agreement with the one obtained by XRD data refinement (~15%). For $MgFe_2O_4$ compound, the situation appears more complex: in addition to the two expected iron populations (O_h and T_d) relating to the AF ordered phase, a third population relating to iron in octahedral or tetrahedral site associated to the quadrupolar doublet indicates the occurrence of a paramagnetic fraction of the compound as mentioned above. Here, the inversion rate calculation leads to a value (59%), which is much lower than the one expected according to the XRD refinement results (79%). Nevertheless, one may notice that both these two techniques are only semi-quantitative and both associated with large uncertainties: quick counting time, presence of a quadrupolar doublet linked to the super-paramagnetism can lead to errors for Mössbauer, refinement with constraint on occupancy factors and refinement of a global B_{iso} on each crystallographic site can also lead to deviation for XRD technique.

In spite of presence of super-paramagnetism for $MgFe_2O_4$, this latter clearly exhibits an anti-ferromagnetic behavior whereas $ZnFe_2O_4$ is paramagnetic, even if the occurrence of local AF interactions between two cations

Table 1
Powder Rietveld refinements results of α-Fe_2O_3, $ZnFe_2O_4$ and $MgFe_2O_4$ compounds

$MgFe_2O_4$ (*Fd*-3*m*)		Crystallite size = 82(7) nm				
$a = 8.39298\ (8)$ Å		$R_p = 2.73\%$		$R_{wp} = 3.46\%$		$R_{Bragg} = 3.55\%$
Atom	Site	x	y	z	B_{iso}	Occupancy
Mg1	8*a*	$\frac{1}{8}$	$\frac{1}{8}$	$\frac{1}{8}$	0.539(52)	0.210(6)
Fe1	8*a*	$\frac{1}{8}$	$\frac{1}{8}$	$\frac{1}{8}$	0.539(52)	0.790(6)
Mg2	16*d*	$\frac{1}{2}$	$\frac{1}{2}$	$\frac{1}{2}$	0.426(46)	0.395(3)
Fe2	16*d*	$\frac{1}{2}$	$\frac{1}{2}$	$\frac{1}{2}$	0.426(46)	0.605(3)
O	32*e*	0.25595(16)	0.25595(16)	0.25595(16)	0.487(62)	1
Score = 1.9996 (Berar's formula)						
$ZnFe_2O_4$ (*Fd*-3*m*)		Crystallite size = 165(5) nm				
$a = 8.44156\ (4)$ Å		$R_p = 2.24\%$		$R_{wp} = 2.86\%$		$R_{Bragg} = 2.27\%$
Atom	Site	x	y	z	B_{iso}	Occupancy
Zn1	8*a*	$\frac{1}{8}$	$\frac{1}{8}$	$\frac{1}{8}$	0.406(39)	0.860(8)
Fe1	8*a*	$\frac{1}{8}$	$\frac{1}{8}$	$\frac{1}{8}$	0.406(39)	0.140(8)
Zn2	16*d*	$\frac{1}{2}$	$\frac{1}{2}$	$\frac{1}{2}$	0.465(44)	0.070(4)
Fe2	16*d*	$\frac{1}{2}$	$\frac{1}{2}$	$\frac{1}{2}$	0.465(44)	0.930(4)
O	32*e*	0.25963(18)	0.25963(18)	0.25963(18)	0.811(61)	1
Score = 1.7529 (Berar's formula)						
Fe_2O_3 (*R*-3*c*)		Crystallite size = 58(5) nm				
$a = 5.03594(5)$ Å $c = 13.74439(15)$ Å		$R_p = 2.01\%$		$R_{wp} = 2.57\%$		$R_{Bragg} = 3.26\%$
Atom	Site	x	y	z	B_{iso}	Occupancy
Fe1	12*c*	0	0	0.35528(5)	0.35	1
O	18*e*	0.30711(33)	0	1/4	0.74	1
Score = 1.6359 (Berar's formula)						

Table 2
Average oxygen–cation distances and estimated crystal fields in hematite α-Fe_2O_3 and spinel ferrites $MgFe_2O_4$ and $ZnFe_2O_4$

	$MgFe_2O_4$	$ZnFe_2O_4$	α-Fe_2O_3
O–M distance [4] (Å)	1.9036(15) [× 4]	1.9685(16) [× 4]	
O–M distance [6] (Å)	2.0495(15) [× 6]	2.0323(16) [× 6]	2.118 (12) [× 3] 1.941 (09) [× 3]
Crystal fields (eV)	$\Delta_{[T_d]} = 1.1$ eV/$\Delta_{[O_h]} = 1.7$ eV	$\Delta_{[T_d]} = 1.0$ eV/$\Delta_{[O_h]} = 1.9$ eV	$\Delta_{[O_h]} = 1.5$ eV

cannot be rejected. These last points will be considered for the interpretation of the reflectivity spectra hereafter presented.

3.3. Diffuse reflectance studies

In both types of compounds, all the optical bands detected in the visible and infrared region can be attributed to intra or inter-atomic transitions involving the Fe^{3+} cation, because electronic transitions implying Mg^{2+} or Zn^{2+} orbitals are known to be only at the origin of charge transfers in the UV region. Whatever the studied composition, their intense reddish color is due to a nearly total absorption of the high-energy part of the visible spectrum (400–550 nm) and, on the opposite, an important diffuse reflectance window in the low-energy part of the visible spectrum (550–800 nm). For the three compositions, diffuse reflectance curves are reported in Fig. 3.

In literature, the absorption bands observed in the UV–vis–NIR range for iron-rich oxides are often explained in a "pure spectroscopic approach" [10,29–36], considering only *d–d* intra-atomic transitions based on Tanabe–Sugano diagram [32]. Indeed, a large number of transitions can occur with a d^5 configuration in octahedral coordination: $^6A_{1g} \rightarrow {}^4T_{1g}$; $^6A_{1g} \rightarrow {}^4T_{2g}$ are often observed in visible range or at the frontier between visible and NIR region. Various band attributions can be found in literature. Nevertheless, one should have to note the Laporte selection rules do not verify this spin state evolution. Indeed, in octahedral field, all transitions from the $^6A_{1g}$ ground state to the excited

crystal-field states are both spin ($\Delta S = 1$) and parity ($\Delta L = 0$) forbidden. In literature, the intense intra-atomic transitions of hematite are then explained because of the local AF coupling between two nearest neighbors Fe^{3+}. Indeed, the AF coupling can suppress the spin forbidden state: considering two neighboring Fe^{3+} which have various spin-up/spin-down distributions, the spin parity of the iron pairs can remain the same in the excited state. In this way, Rossman [32] observes that the intensity of the absorption bands increases with the formation of iron chains, clusters or extended networks, with strong magnetic interactions. On the contrary, here it is claimed that the absorption bands of the iron-rich oxides do not only result from CF transitions. Indeed, various points in contradiction with a pure crystal-field model can be mentioned. Firstly, the intense absorption bands occur with quite the same intensity for both anti-ferromagnetic and paramagnetic compounds ($MgFe_2O_4$ or $ZnFe_2O_4$, respectively, as Mössbauer previous study has shown). This is in complete contradiction with the relationship between the magnetic ordering and the color of the Fe^{3+}-based compounds described in the literature, even if, one could argue that from a local point a view, anti-ferromagnetic dimmers could still exist in the zinc compound. Secondly, taking into account the low third ionization energies corresponding to Fe^{3+} ion as well as electronic configuration $3d^5$ ($S = 5/2$) of the high-spin state, charge transfer such as $O^{2-} + Fe^{3+} \rightarrow O^{-} + Fe^{2+}$ has a high probability to occur in visible range (1.5–3 eV) compared to intra-atomic d–d transitions. Finally, hematite and Fe^{3+} spinel compounds exhibit reversible thermochromism, changing from reddish-brown to black with a darker and darker color versus temperature. This color change is mostly associated with charge transfers and not with d–d transitions since it can be observed for the semi-conductors with wide band gap such as ZnO, Bi_2O_3, TiO_2, CeO_2, etc. In literature, such a shift versus temperature roughly around 0.1 eV/100 °C—is clearly associated with the thermal expansion of the unit cell and so the increase of metal–oxygen bond distances. On the other hand, one can argue that crystal field decreases with metal–oxygen lengths and such a reduction

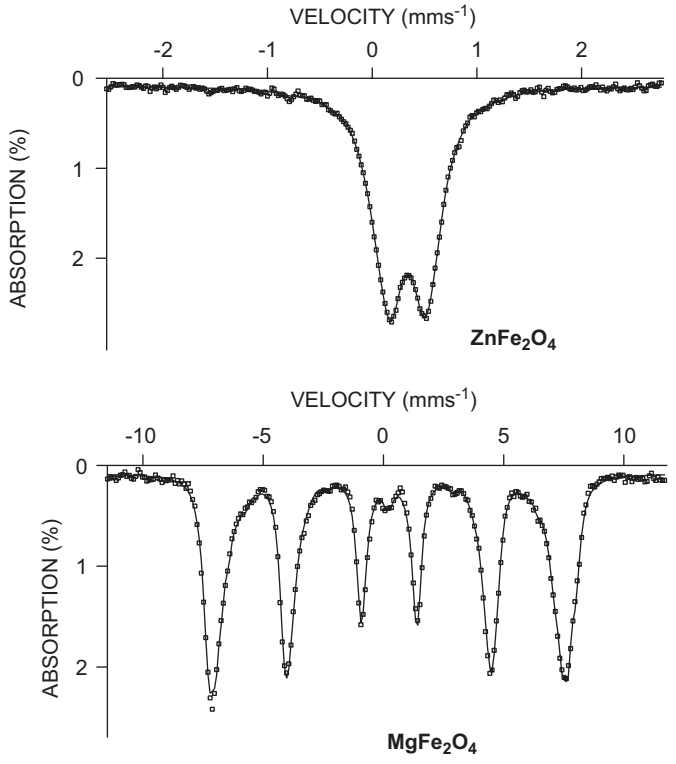

Fig. 2. Room temperature Mössbauer spectra of $ZnFe_2O_4$ and $MgFe_2O_4$ spinels. The calculated spectrum is represented by the full line.

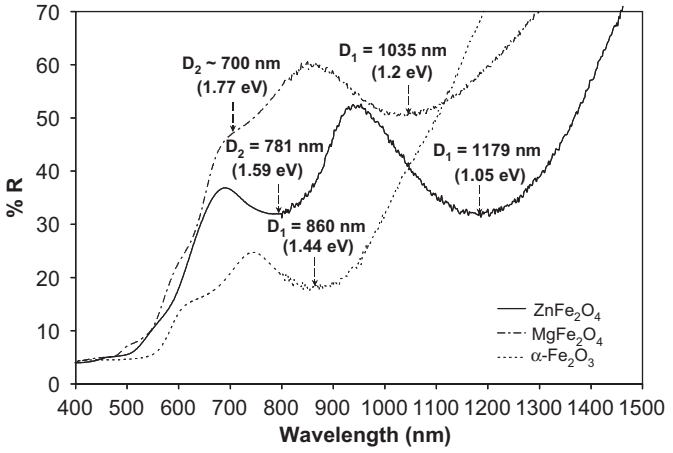

Fig. 3. Diffuse reflectance vis–NIR spectra of α-Fe_2O_3, $ZnFe_2O_4$ and $MgFe_2O_4$ compounds. Only large absorption bands (D_1 and D_2) have been pointed out.

Table 3
Hyperfine parameters obtained from refinements at room temperature of Mössbauer spectra relating to spinel ferrites

Compound	Distribution	δ (mm/s)	Γ (mm/s)	ε (mm/s)	Δ (mm/s)	H (T)	%	Iron site
$MgFe_2O_4$	1	0.28	0.40	−0.001	–	45.2(5)	59(1)	Fe^{3+} [T_d]
	2	0.33	0.40	0.034	–	42.9(5)	35(1)	Fe^{3+} [O_h]
	3	0.24	0.40	–	1.4(3)	–	6(1)	Fe^{3+} [O_h]
$ZnFe_2O_4$	1	0.22	0.25	–	0.60(5)	–	11(1)	Fe^{3+} [T_d]
	2	0.35	0.25	–	0.38(5)	–	89(1)	Fe^{3+} [O_h]
Fe_2O_3	1	0.37	0.27	−0.115		51.5(2)	100	Fe^{3+} [O_h]

ε: quadrupolar splitting.

could also influence the absorption spectra. However, considering the Tanabe–Sugano diagram for a $3d^5$ ion in octahedral symmetry and with a high-spin state (low CF), the crystal-field reduction should be associated with an increase of the E/B transition energy value and, experimentally the reverse phenomenon is here observed.

Hence, for all above reasons, the two more intense absorption bands in the visible range can be attributed without any doubt to two charge transfers. For supporting discussion, an enlargement of the reflectance spectra in visible region is reported in Fig. 4, while the associated first derivative curves of this enlargement are shown in Fig. 5. For all the three compounds, the double charge transfer phenomenon attributed to a ligand-to-metal $2p(O^{2-})\rightarrow 3d(Fe^{3+})$ transfer, exhibits absorption edges, which are noted CT_1 and CT_2, at around 2 eV. Moreover, the diffuse reflectance curves of the two spinel compounds $MgFe_2O_4$ and $ZnFe_2O_4$ clearly exhibit two additional broad absorption bands, which can be attributed without any doubt, from their pseudo-Gaussian shape, to Fe^{3+} d–d intra-atomic transitions. These two bands, called hereafter D_1 and D_2, are centered at about 1180 and 780 nm for $ZnFe_2O_4$ and at about 1035 and 700 nm for $MgFe_2O_4$. For α-Fe_2O_3 hematite, only one broad absorption band centered at about 860 nm is clearly distinguished. One can think that in the spinel structures, the two d–d transition bands are related to octahedral and tetrahedral crystal-field transitions while in hematite, only the octahedral crystal-fields exist. Nevertheless, the intensities of both these bands, which are more important in zinc compound than in magnesium one where the iron rate in tetrahedral site is significantly higher, clearly show that the two phenomena are only due to transitions involving Fe^{3+} in octahedral sites. D_1 and D_2 have been identified as ${}^6A_{1g}\rightarrow{}^4T_{1g}$ and ${}^6A_{1g}\rightarrow{}^4T_{2g}$ energetic states from Tanabe–Sugano diagram as shown by previous studies [31]. For the two spinel-type compounds, according to the Tanabe–Sugano diagram for a d^5 configuration in $[O_h]$ symmetry, by considering the lowest energy band (D_1) as ${}^6A_{1g}\rightarrow{}^4T_{1g}$ transition (1180 and 1035 nm for $ZnAl_2O_4$ and $MgAl_2O_4$, respectively) and the Racah parameter [37] $B = 650\,cm^{-1}$, the calculated energies corresponding to the ${}^6A_{1g}\rightarrow{}^4T_{2g}$ transition (790 and 720 nm for $ZnFe_2O_4$ and $MgFe_2O_4$, respectively) are in good agreement with the experimentally detected D_2 bands (781 and 700 nm). Then, the octahedral crystal fields can be

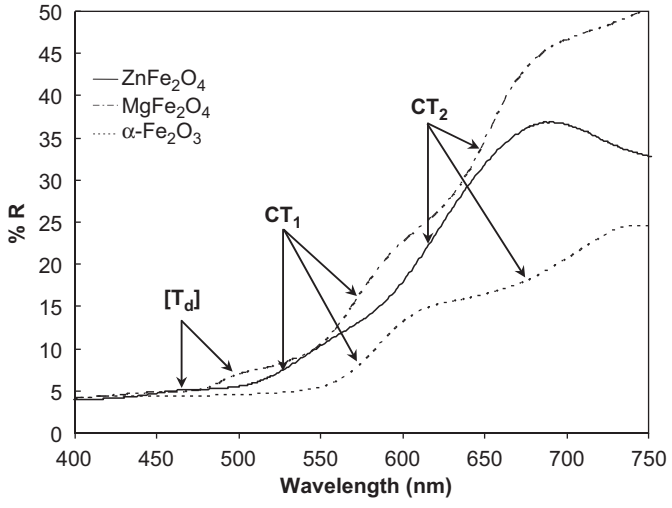

Fig. 4. Diffuse reflectance visible spectra of α-Fe_2O_3, $ZnFe_2O_4$ and $MgFe_2O_4$ compounds. CT_1 and CT_2: $O(2p)\rightarrow Fe(3d)$ charge transfer in octahedral site; $[T_d]$: $O(2p)\rightarrow Fe(3d)$ charge transfer in tetrahedral site.

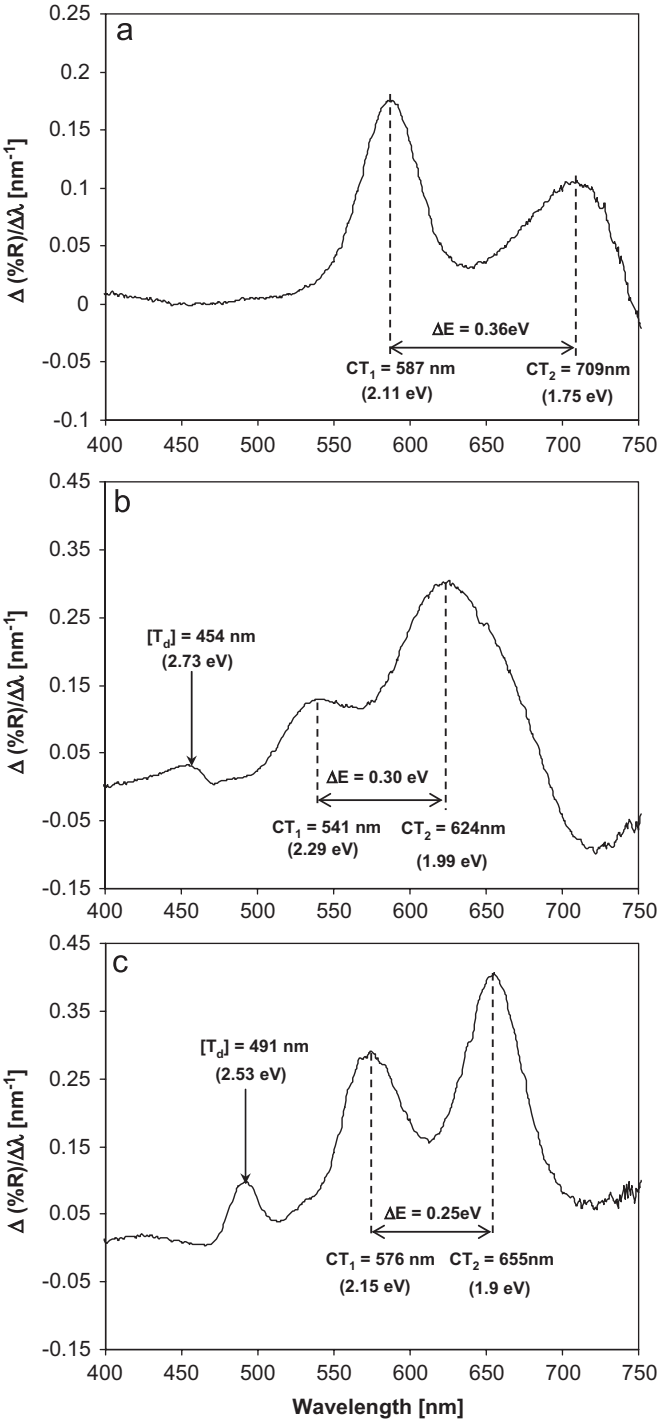

Fig. 5. Derivative curves from diffuse reflectance data of (a) α-Fe_2O_3, (b) $ZnFe_2O_4$ and (c) $MgFe_2O_4$ compounds.

extracted from this diagram: they have been calculated equal to 1.9 and 1.7 eV for $ZnFe_2O_4$ and $MgFe_2O_4$, respectively, values in good agreement with previous studies [37]. By applying the same identification method to the hematite sample considering same Racah parameter values than for D_1 band, the non-detected $^6A_{1g} \rightarrow {}^4T_{2g}$ transition state should appear at about 640 nm. This D_2 band is hidden by $O^{2-} \rightarrow Fe^{3+}$ charge transfers. The hematite crystal field was then roughly estimated at 1.5 eV, which is also consistent with literature [38,39]. At this stage of the study, the extracted crystal field for the three compounds can be discussed in a comparative way. The crystal-field energy of Fe^{3+} octahedra can be influenced by (i) the octahedron size (i.e. the average iron–oxygen bonds length), (ii) the octahedron distortion related to the symmetry point group of the site and (iii) the electronegativity of the ligands. In these compounds, the rate of octahedral site occupied by iron cation is high (60% for $MgFe_2O_4$, 93% for $ZnFe_2O_4$, 100% in α-Fe_2O_3). For such high Fe^{3+} rates in octahedral site, the Fe^{3+} octahedra size remains almost equivalent in each structure. Moreover, in a first approximation, higher the trigonal distortion of the octahedral sites, lower the crystal-field energy. Indeed, C_{3v} and D_{3d} symmetry point groups exhibit in comparison with O_h point group a more spherical character associated to a lower crystal field. Compared to the D_{3d} symmetry, the C_{3v} one leads to the lowest crystal field. This is in agreement with the estimated crystal-field values. Nevertheless, it is difficult to explain the difference between the crystal-field energies for the two spinels considering only the distortion of octahedral site. The more satisfying explanation to interpret the crystal field of α-Fe_2O_3 (1.5 eV), $MgFe_2O_4$ (1.7 eV) and $ZnFe_2O_4$ (1.9 eV) is based on the partial charge density of ligands due to the Fe–O and M–O (M = Mg, Zn) competitive bonds. Indeed, magnesium (1.3) exhibits the weakest Pauling' scale electronegativity compared to zinc (1.7) and iron (1.9). The very low electronegativity of magnesium involves highly polarized Mg–O bonds (ionic bonds) and consequently, the associated crystal field around Fe^{3+} inside $MgFe_2O_4$ spinel is lower than inside $ZnFe_2O_4$. Moreover, the crystal fields related to T_d sites have been estimated on the basis of the crystal fields in octahedral sites and the respective bond distances of O_h and T_d sites.

In a last part, a correlation between oxides structural features and the energetic difference (ΔE) between the two O–Fe charge transfers has been proposed. In corundum structure and in spinel compounds, [FeO_6] octahedra exhibit a C_{3v}-type distortion and adopt a D_{3d} point group, respectively. Then, the crystal-field splitting is also affected by the trigonal distortion leading for D_{3d} and C_{3v} point groups to three separated energy levels; in these cases, in comparison to the energy level degeneracy inside O_h configuration in two levels ($t_2 = d_{xy}$, d_{zy}, d_{xz} and $e = d_{z2}$, d_{x2-y2}), an additional splitting of t_2 occurs, following character table [40]. A double charge transfer appears, one between oxygen and the less energetic t_2 orbital(s) and the other one between oxygen and the more energetic t_2 orbital(s). From the diffuse reflectance curve, this t_2 energy splitting, equal to ΔE, is equal to 0.36, 0.25 and 0.30 eV for hematite, $MgFe_2O_4$ and $ZnFe_2O_4$ spinels, respectively. Indeed, the two ligand-to-metal transfers are located at about 587/709, 576/655 and 541/624 nm for hematite, $MgFe_2O_4$ and $ZnFe_2O_4$, respectively, as shown in Fig. 5. From group theory, the ΔE splitting value should be directly linked to the iron octahedral distortion. Here indeed, the hematite which exhibits the most important distortion with two sets of Fe–O bond lengths is associated with the most important ΔE. Between the two spinels, based on XRD refinement results (oxygen atomic positions, $x = 0.25$ for a regular O_h site), the average octahedral site of magnesium ferrite is largely more isotropic than the zinc ferrite one (Table 1). Then, the calculated ΔE appears consistent. Moreover, for spinel ferrites, a third ligand-to-metal charge transfer, associated here to a tetrahedral site bond, is clearly detected from derivative curves (Figs. 5b and c) at slightly higher energies than the two previous ones. The wavelength position of this third charge transfer is about 490 and 454 nm for $MgFe_2O_4$ and $ZnFe_2O_4$, respectively. As expected, in [FeO_4] tetrahedra, O^{2-}–Fe^{3+} bonds are shorter than in [FeO_6] octahedra and consequently the associated charge transfer is more energetic. It can be pointed out that the absorption intensity of this charge transfer, largely more important for $MgFe_2O_4$ than for $ZnFe_2O_4$, seems well related to the inversion rates preliminary characterized by X-ray data analysis.

In order to summarize all above results, the various absorption phenomena occurring in UV–visible region and related electronic transitions are schematically represented in Fig. 6. Here, the $O^{2-} \rightarrow Fe^{3+}$ CT bands as well as the various CF transitions are reported for each studied compound; $ZnFe_2O_4$ spinel, $MgFe_2O_4$ spinel and α-Fe_2O_3 hematite.

4. Conclusion

Herein, the identification of Fe^{3+} crystal-field transitions (CF bands) in NIR region allows estimating crystal fields in the series of compounds here studied (Fe_2O_3, $MgFe_2O_4$ and $ZnFe_2O_4$): crystal field decreases with the increase of the octahedral site trigonal distortion and the reduction of the Fe–O bond ionicity. Nevertheless, the most important point is the origin of the dark red coloration of Fe^{3+}-based spinels and hematite which is mainly due to ligand-to-metal charge transfers bands (CT). Indeed, taking into account the CF bands intensities, the very broad and intense absorption phenomena in the visible region can be only attributed to a double CT resulting from the trigonal distortion inducing the occurrence of t_{2g} orbital splitting. A strong argument in favor of our consideration is the red-shift observed during the heating of the material; a blue shift is predicted if these bands would correspond to CF transitions involving Fe^{3+} ions. Then, the structural

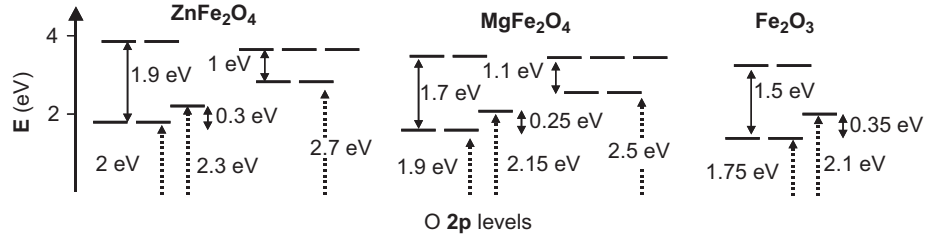

Fig. 6. Schematic bands diagrams with inter-atomic electronic transfers in hematite and spinel ferrite compounds. CT_1, CT_2 and $[T_d]$: inter-atomic transfers between oxygen atomic $2p$-orbitals and iron atomic $3d(t_{2g})$-orbitals.

consideration of the various Fe^{3+}-based oxides here studied, has allowed explaining the optical absorption properties in visible as well as NIR regions. A schematic band diagrams where all the observed electronic transitions are reported can be proposed. It allows for each compound a precise positioning of the oxygen $2p$ and iron $3d$ levels.

This work which is the first-one to our knowledge to achieve a complete interpretation of the optical properties of iron-rich oxides, opens the possibility to modify the coloration of the crystalline Fe^{3+}-based oxides. Indeed, this study showed that the Fe^{3+} local environment, i.e. coordination, size and distortion of the Fe^{3+} site as well as Fe–O bond ionicity lead to control the d iron energy levels and the optical band gap positioning and so, the oxide coloration.

References

[1] A.L. Peter (Ed.), Pigment Handbook, Wiley, New York, 1987.
[2] R.M. Cornell, U. Schwertman, The Iron Oxides: Properties, Reactions, Occurrence, and Uses, VCH, Weinheim, Germany, 1996, pp. 1–25.
[3] H. Katsuki, S. Komarneni, J. Am. Ceram. Soc. 86 (1) (2003) 183–185.
[4] 〈www.danielsmith.com〉.
[5] G.Q. Yang, et al., Dyes Pigments 55 (2002) 9–16.
[6] K. Koshizuka, R. Tamaru, Iron oxide (Fe_2O_3), in: A. Kato, T. Yamaguchi (Eds.), New Ceramics Powder Handbook, Science Forum, Tokyo, Japan, 1983, pp. 156–168 (Chapter 11).
[7] P.A. Lessing, Am. Ceram. Soc. Bull. 68 (1989) 1002.
[8] M. Kakihana, et al., J. Sol-Gel Sci. Technol. 12 (1998) 95.
[9] M. Elias, et al., Mater. Sci. Eng. B 127 (2006) 70–80.
[10] D.M. Sherman, T.D. Waite, Am. Mineral. 70 (1985) 1262–1269.
[11] N. Pechini, Patent no. 3,330, 1967, p. 697.
[12] M. Loan, G.M. Parkinson, W.R. Richmond, Am. Mineral. 90 (2005) 258–261;
Y. Cudennec, A. Lecerf, J. Solid State Chem. 179 (3) (2006) 716–722.
[13] M. Pourbaix, in: Gauthier-Villars (Ed.), Atlas d'équilibres électrochimiques à 25 °C, Paris, France, 1963.
[14] H.M. Rietveld, J. Appl. Crystallogr. 2 (1969) 65–71;
H.M. Rietveld, Acta Crystallogr. 22 (1967) 151–152.
[15] J. Rodriguez-Carvajal, 1990, FULLPROF: a program for Rietveld refinement and pattern matching analysis, in: Abstracts of the Satellite Meeting on Powder Diffraction of the XV Congress of the IUCr, Toulouse, Grenoble, France, p. 127.
[16] J. Hesse, A. Rubartsch, J. Phys. E-Sci. Instrum. 7 (1974) 526.
[17] R.J. Hill, et al., Phys. Chem. Minerals 4 (1979) 317–340.
[18] J.S. Smart, Phys. Rev. 93 (1954) 847–850.
[19] P. Porta, et al., J. Solid State Chem. 11 (1974) 135–147.
[20] V.G. Tsirel'son, et al., Dokl. Akad. Nauk SSSR 298 (1988) 1137.
[21] L.P. Keller, G.J. McCarthy, ICDD grant-in-aid, North Dakota State University, Fargo, North Dakota, USA, 1984.
[22] Natl. Bur. Stand. (US) Monogr. 25(9) (1971) 60.
[23] E.N. Maslen, et al., Acta Crystallogr. B 50 (1994) 435–441.
[24] H.St.C. O'Neill, Eur. J. Mineral. 4 (1992) 571–580.
[25] G.M. Kalvius, et al., Mater. Sci. Forum 321 (2000) 802–807.
[26] G.E. Bacon, F.F. Roberts, Acta Crystallogr. 6 (1953) 57–62.
[27] H.St.C. O'Neill, et al., Am. Mineral. 77 (1992) 725–740.
[28] U. König, G. Chol, J. Appl. Crystallogr. 1 (1968) 124–126.
[29] A. Herpin (Ed.), Théorie du Magnetisme, Presses Universitaires de France, Paris, 1968.
[30] S.A. Oliver, et al., Scr. Metall. Mater. 33 (1995) 1695–1701.
[31] L. Wang, et al., Phys. Status Solidi (b) 241 (2) (2004) 377–382.
[32] G.R. Rossman, in: M.D. Dyar, C. McCammon, M.W. Schaefer (Eds), The Geochemical Society, Special Publication no. 5, 1996.
[33] J. Torrent, V. Barron, Clays Clay Miner. 51 (3) (2003) 309–317.
[34] C.S. Kosmas, et al., Clays Clay Miner. 34 (6) (1986) 625–634.
[35] R.V. Morris, et al., J. Geophys. Res. 97 (1992) 10257–10266.
[36] R.A. Candeia, et al., Mater. Res. Bull. 41 (2006) 183–190.
[37] S.F. Alvarado, et al., Phys. Rev. B 14 (7) (1976) 2740–2745.
[38] T. Droubay, S.A. Chambers, Phys. Rev. B 64 (2001) 205414.
[39] Z.W. Zhang, et al., Phys. Rev. B 48 (22) (1993) 16407–16409.
[40] J.E. Huheey, E.A. Keiter, R.L. Keiter, The crystal field theory, in: De Boeck Université (Ed.), Inorganic Chemistry: Principles of structure and reactivity, Belgium, Bruxelles, 1996, pp. 397–399 (Chapter 11).